

Rotational evolution of young-to-old stars with data-driven three-dimensional wind models

D. Evensberget ^{1*}, A. A. Vidotto ¹,

¹*Leiden Observatory, Leiden University, PO Box 9513, 2300 RA Leiden, The Netherlands*

Accepted XXX. Received YYY; in original form ZZZ

ABSTRACT

Solar-type stars form with a wide range of rotation rates Ω . A wide Ω range persists until a stellar age of $t \sim 0.6$ Gyr, after which solar-type stars exhibit Skumanich spin-down where $\Omega \propto t^{-1/2}$. Rotational evolution models incorporating polytropic stellar winds struggle to simultaneously reproduce these two regimes, namely the initially wide Ω range and the Skumanich spin-down without imposing an a-priori cap on the wind mass-loss rate. We show that a three-dimensional wind model driven by Alfvén waves and observational data yields wind torques that agree with the observed age distribution of Ω . In our models of the Sun and twenty-seven open cluster stars aged from 0.04 to 0.6 Gyr that have observationally derived surface magnetic maps and rotation rates, we find evidence of exponential spin-down in young stars that are rapid rotators and Skumanich spin-down for slow rotators. The two spin-down regimes emerge naturally from our data-driven models. Our modelling suggests that the observed age distribution of stellar rotation rates Ω arises as a consequence of magnetic field strength saturation in rapid rotators.

Key words: stars: winds, outflows – stars: rotation – stars: magnetic field – stars: solar-type – stars: evolution – Sun: evolution

1 INTRODUCTION

Solar-type (FGK) stars enter the stellar spin-down era with a wide range of rotation rates Ω (Stauffer et al. 1985; Bouvier 1991; Edwards et al. 1993). The fastest rotators spin near the stellar break-up velocity and the slowest rotators are up to two orders of magnitude slower (Gallet & Bouvier 2013). Observations of stellar clusters show that this wide range of periods is eventually lost; some mechanism harmonises their rotation rates by the onset of the spin-down era at an age $t_s \sim 0.6$ Gyr (Skumanich 1972), after which $\Omega \propto t^{-1/2}$. To reproduce the observed Ω distribution, spin-down models have incorporated a ‘knee’ in the $\dot{\Omega}(\Omega)$ relation (e.g. Stauffer & Hartmann 1987; Chaboyer et al. 1995; Krishnamurthi et al. 1997), so that $\dot{\Omega} \propto \Omega$ for rapid rotators and $\dot{\Omega} \propto \Omega^3$ for slow rotators as required to attain Skumanich spin-down (e.g. Durney & Latour 1978).

Solar-type stars spin-down by means of magnetised stellar winds (e.g. Parker 1958; Schatzman 1962) both before and during the Skumanich spin-down era. From one-dimensional models, we can write the wind torque as $\dot{J} \propto M\Omega R_A^n$ where \dot{M} is the wind mass-loss rate and R_A is the Alfvén radius (Weber & Davis 1967; Mestel 1968, 1984; Kawaler 1988). Mass-loss rate saturation in rapid rotators (e.g. Cranmer & Saar 2011) can be imposed to produce the required knee in the $\dot{\Omega}(\Omega)$ relation. In polytropic magnetohydrodynamic wind models (Vidotto et al. 2009; Matt et al. 2012; Réville et al. 2015; Finley & Matt 2017; Finley et al. 2018), the wind mass loss rate is governed largely by the coronal temperature and wind density. By varying the wind density, and thus \dot{M} , models are able to match spin-down ‘gyrotracks’ $\Omega(t)$ found by integrating $\dot{\Omega}$ to observational data (Gallet & Bouvier 2013; Johnstone et al. 2015; Sadeghi

Ardestani et al. 2017). This mass loss rate saturation is, however, externally imposed on the wind model. In contrast to polytropic wind models, an Alfvén wave based wind model (Sokolov et al. 2013; van der Holst et al. 2014) can shift the wind model boundary downwards into the much colder and denser stellar chromosphere, and compute the coronal wind density and \dot{M} consistently with \dot{J} and R_A (e.g. Garraffo et al. 2015; Alvarado-Gómez et al. 2016; Cohen 2017).

In this letter, we show that the resulting $\dot{\Omega}$ of the Sun and a set of twenty-seven young, solar-type cluster stars aged from ~ 40 Myr to ~ 600 Myr (Evensberget et al. 2021, 2022, 2023) appears compatible with the observed age distribution of stellar rotation rates Ω (Gallet & Bouvier 2013) for a solar mass star without imposing any a priori assumptions about mass loss saturation. In Section 2, we show this by comparing instantaneous wind torque \dot{J}_w of our models to a simple observation-based gyrotrack model based on the work of Gallet & Bouvier (2013) containing hundreds of rotation rates. The resulting wind torques do however need to be scaled by a factor of ~ 7 in order to yield the expected Skumanich spin-down rate at solar maximum conditions, as presented in Section 3. This scaling factor is the only free parameter in our calculated wind torques. In Section 4 we present our conclusions.

2 WIND TORQUE MODEL

In our recent work we have modelled the winds of thirty young, solar-type stars (Evensberget et al. 2021, 2022, 2023) with well characterised ages, and whose surface magnetic fields have previously been mapped with Zeeman-Doppler imaging (ZDI) by Folsom et al. (2016, 2018). The modelled stars are part of the Hyades, Coma Berenices, Hercules-Lyra, Pleiades, AB Doradus, and Columba-Horologium-

* E-mail: evensberget@strw.leidenuniv.nl

Tucana clusters¹. As cluster members, these stars' ages are known to within 5% to 20%. For reference the stars' ages, rotation rates, masses and radii are given in Table 1. This is the largest sample of stars with well characterised ages and ZDI surface magnetic fields derived with a consistent methodology.

For each star a wind model was obtained by letting the surface magnetic field drive a three-dimensional numerical wind model (Powell et al. 1999; Tóth et al. 2012) incorporating Alfvén wave coronal heating (Sokolov et al. 2013; van der Holst et al. 2014). The resulting wind solutions permit us to simultaneously compute consistent key quantities such as wind mass loss rate \dot{M}_w and wind angular momentum loss rate \dot{J}_w as described in Appendix A. Identical solar parameter values are used in all the wind models; the only varying parameters are the surface magnetic map, stellar rotation rate, mass, and radius as indicated in Table 2.

2.1 Rotational braking from wind torques

The stellar spin-down rates $\dot{\Omega}_w$ are computed from (scaled) wind torques \dot{J}_w that we previously published (Evensberget et al. 2023). In this paper we apply a scaling factor of 7 to our stellar and solar \dot{J}_w values to match the expected Skumanich spin-down rate at solar maximum conditions.

To compute spin-down rates from wind torques, we use the stellar rotational inertia values I from Baraffe et al. (2015). As $J = \Omega I$ we get (e.g. Johnstone et al. 2015; Matt et al. 2015)

$$\dot{\Omega}_w = \dot{J}_w / I - \Omega \dot{I} / I \quad (\text{Stellar wind models}) \quad (1)$$

where \dot{J}_w is the wind torque and $\Omega \dot{I}$ is the contraction torque (Gallet & Bouvier 2015). In the Baraffe et al. models I is essentially steady by $t \sim 100$ Myr so that the wind torque term dominates $\dot{\Omega}_w$. For convenience, the I and values used are given in Appendix B. In Fig. 1 the stellar rate of rotation is plotted against the stellar age (coloured circles). The stellar spin-down rates $\dot{\Omega}_w$ derived from our wind models are shown as coloured arrow attached to the symbol of each star, and pointing in the direction of $\dot{\Omega}_w$.

To guide the eye, the shaded region of Fig. 1 shows the range between the 25th and 90th percentile of observed Ω values (curves from Gallet & Bouvier 2013). The pre-Skumanich spin-down era may be identified as the time where there is significant difference between the two percentiles (up to $t \sim 600$ Myr). This era is followed by the Skumanich spin-down era where $\Omega \propto t^{-1/2}$. From Fig. 1 we have good coverage of the Gallet & Bouvier (2013) sample around 0.1 Gyr and 0.6 Gyr, however our ZDI dataset has no stars between onset of the Skumanich relation and the solar models.

2.2 Rotational braking from cluster spin rates

Gallet & Bouvier (2013) fitted $\Omega(t)$ curves, so-called ‘gyrotracks’, to the observed rotation rates of young and very young ($t < 30$ Myr) clusters, incorporating mass loss saturation, core-envelope decoupling, and other effects. recently *GAIA* data has been used to infer the age distribution of rotation rates for a much larger sample of stars. The essential features of the revised gyrotracks are however retained (e.g. Godoy-Rivera et al. 2021, Fig. 13) in the age and mass

range where we have wind model data. Here, we fit a very simple model on the form

$$\dot{\Omega}_{\text{obs}} = \begin{cases} -k_1 \Omega, & \Omega > \Omega_{\text{sat}} \\ -k_2 \Omega^3, & \Omega \leq \Omega_{\text{sat}} \end{cases}, \quad (\text{Vector field}) \quad (2)$$

to the observation-based Gallet & Bouvier (2013) 25th and 90th percentile $\Omega(t)$ gyrotrack curves, focusing on the spin-down era $30 \text{ Myr} < t < 4.6 \text{ Gyr}$ for a one solar mass star². We note that much of the signal for solar analogues is in stars less than 100 Myr old (Denissenkov et al. 2010; Gallet & Bouvier 2013, 2015).

Our simplified model (2) permits gyrotracks $\Omega_{\text{obs}}(t)$ to decay exponentially when $\Omega > \Omega_{\text{sat}}$, while adhering to the Skumanich (1972) relation $\Omega(t) \propto t^{-1/2}$ for $\Omega < \Omega_{\text{sat}}$. We have parametrised the pre-Skumanich spin-down era in terms of an exponential decay constant k_1 so that the rotational spin-down timescale in this era $\Omega/\dot{\Omega}_{\text{obs}} = k_1^{-1} = 120 \text{ Myr}$. The value of k_2 is then found by matching the solar age and angular velocity: $k_2 = \frac{1}{2} \Omega_{\odot}^{-2} t_{\odot}^{-1} = 4.1 \times 10^{-7} \text{ s rad}^{-2}$. From continuity of $\dot{\Omega}_{\text{obs}}$ the saturation threshold is $\Omega_{\text{sat}} = \sqrt{k_1/k_2}$. This gives a reasonable $\Omega_{\text{sat}} = 8.9 \Omega_{\odot}$, given that this parameter can vary between $3 \Omega_{\odot}$ and $15 \Omega_{\odot}$ depending on model choices (Matt et al. 2015; Amard et al. 2016). In Fig. 1 the resulting $\dot{\Omega}_{\text{obs}}$ values are shown as a vector field (little grey arrows). By design we have excellent agreement between the 25th and 90th percentile $\Omega(t)$ gyrotrack curves (edges of the grey region) and the $\dot{\Omega}_{\text{obs}}$ vector field (grey arrows), indicating that eq. (2) captures the dominant features of the Gallet & Bouvier (2013) spin-down era gyrotracks for a Solar-mass star. In addition to the vector field, we have also added small trailing gyrotrack segments $\Omega_{\text{obs}}(t)$ to each star. By comparing the slope of each stars' trailing trajectory segment $\Omega_{\text{obs}}(t)$ to its emerging arrow $\dot{\Omega}_w$ it can be seen that there is good agreement between the wind torque based spin-down rates and the gyrotrack segments.

As mentioned in Section 2.1, we apply a scaling factor of 7 to the wind torques \dot{J}_w of Evensberget et al. (2023). In our dataset this corresponds to matching the wind torque \dot{J}_w at solar maximum to the Sun's gyrotrack predicted torque \dot{J}_{obs} . The scaling effect can be seen in Fig. 1 where the most downwards-pointing of the wind torque arrows extending from the Sun symbols is in good agreement with the gyrotrack trail. The wind torque scaling is discussed further in Section 3.

2.3 Saturation in rapid rotators

The good agreement between the wind torque based spin-down rates $\dot{\Omega}_w$ (coloured arrows) and the gyrotracks $\Omega_{\text{obs}}(t)$ (coloured trailing curve segments) in Fig. 1 suggests the presence of a saturation effect in the $\dot{\Omega}_w$ values around Ω_{sat} . This is confirmed in Fig. 2 where the top panel shows the calculated spin-down timescale $\Omega/\dot{\Omega}_w$ plotted against the rotation period as coloured symbols, and $\Omega/\dot{\Omega}_{\text{obs}}$ (see equation 2) as a grey curve consisting of two line segments. Vertical distance between the star symbols and the grey curve correspond to trail-arrow mismatch in Fig. 1.

The dashed black curve in each panel shows a fitted broken power law

$$y/y_{\text{sat}} = (\Omega/\Omega_{\text{sat}})^a \quad (3)$$

¹ The β Pictoris stars studied in Evensberget et al. (2023) are excluded from the analysis in this work as their age of $24 \pm 3 \text{ Myr}$ suggests that they are still contracting and have not yet reached the spin-down era.

² The grey band in Fig. 1 is for a $1 M_{\odot}$ star, while many of the stars modelled in this study mass around $0.85 \pm 0.10 M_{\odot}$. We do not expect this to affect the qualitative conclusions in this paper since the gyrotracks are qualitatively similar for a $0.8 M_{\odot}$ star in Gallet & Bouvier (2015).

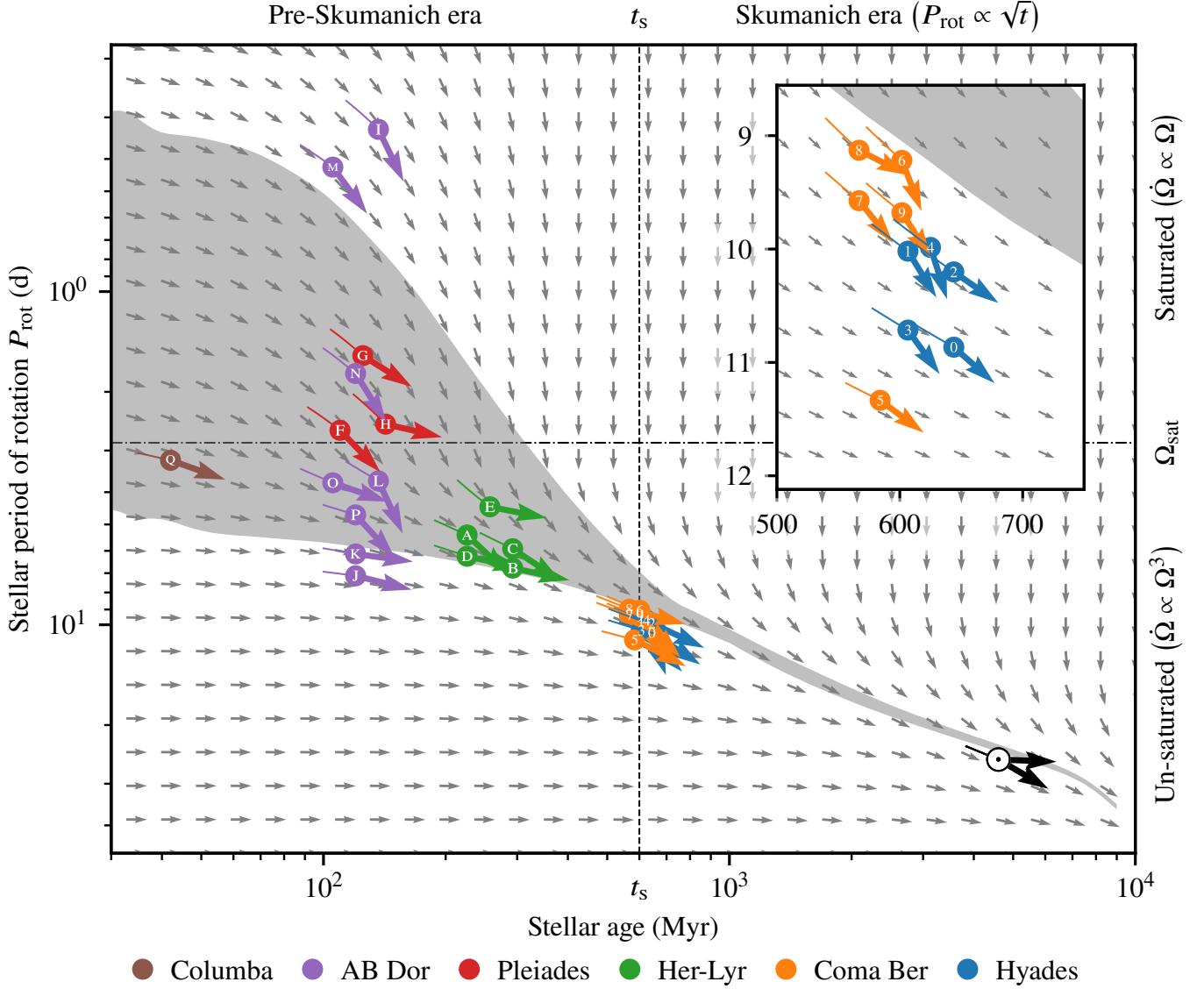


Figure 1. Stellar rotational period and wind-derived spin-down rates $\dot{\Omega}_w$ plotted against stellar age for the stellar wind models in Evensberger et al. (2021, 2022, 2023). The angular velocity of each star is plotted against the star’s age with a coloured symbol. The spin-down rate $\dot{\Omega}_w$ is indicated with an arrow extending from the symbol. Larger values of $\dot{\Omega}_w$ and thus of $\dot{\Omega}_w$ produce more downwards-pointing arrows in the plot. In order for the symbols not to overlap each other we have added a small pseudorandom shift to the stellar ages. As the Hyades and Coma Berenices stars are close together in both Ω and age, we have added an inset in the top right corner which gives a zoomed in view of this region. The Sun symbol and the two black arrows extending from it represent the solar minimum and solar maximum models from Evensberger et al. (2023). In the plot background we have added a shaded region corresponding to the region between the 25th and 90th percentile of stellar $\Omega_{\text{obs}}(t)$ gyrotracks as a function of age for a solar mass star from Gallet & Bouvier (2013). The plot background also contains a vector field (grey arrows) of $\dot{\Omega}_{\text{obs}}$ values from the fitted model described by equation (2). The vertical dashed line denotes the onset of the Skumanich spin-down era, while the horizontal dash-dotted line separates the saturated and un-saturated spin-down regimes as noted in the top and right margins.

in which $\Omega_{\text{sat}} = 8.9 \Omega_{\odot}$ is fixed, while y_{sat} and a are found by simultaneous fitting. The exponent a is permitted to take on a different value on each side of Ω_{sat} . The a and y_{sat} values are given in Table 3, and the a values are annotated in Fig. 2. From its top panel it can be seen that the fitted curve closely matches the observed $\Omega/\dot{\Omega}_{\text{obs}}$ relation of equation (2) shown and annotated in grey.

The middle panel of Fig. 2 show the wind mass loss rate \dot{M}_w plotted against the rotation period. The wind mass loss rate exhibits a similar pattern of saturation (notwithstanding a slightly different scatter) around Ω_{sat} as that of the spin-down timescale. The mass

loss rate \dot{M} appears to saturate for $\Omega > \Omega_{\text{sat}}$ in a similar manner as $\Omega/\dot{\Omega}_w$.

The bottom panel of Fig. 2 shows the surface unsigned magnetic flux $\Phi = 4\pi R^2 B_r$ plotted against the rotation period³. Once again the fitted dashed curve and the scatter have a similar shape those of the preceding panels. Hence both the \dot{M}_w and Φ values exhibit similar trends as the top panel $\Omega/\dot{\Omega}_w$ values, albeit with different slopes and intersections with the range of solar values.

³ By B_r we mean the average strength of the surface radial magnetic field.

Table 1. Relevant model parameters and results from the wind models (Evensberget et al. 2023) used in this work and stellar rotational inertia values. The ‘case’ column denotes the model case number from Evensberget et al. (2023). The ‘type’ column gives the star’s spectral type. When the spectral type is calculated from T_{eff} following Pecaut & Mamajek (2013) this is denoted by a dagger symbol (\dagger). The ‘age’ column gives the stellar age, and the following columns give the stellar mass M , radius R , and rotational period P_{rot} . The B_r value is the average unsigned radial magnetic field over the stellar surface from the Zeeman-Doppler maps of Folsom et al. (2016, 2018), from which the the previous columns values were also taken. The wind mass loss rate \dot{M}_w and wind torque \dot{J}_w are computed from the wind models. A scaling factor of 7 has been applied to the \dot{J}_w values as described in Section 3. In the main text this factor is incorporated into the definition of \dot{J}_w . The rotational inertia I values are taken from the models of Baraffe et al. (2015). The stellar age column can also be used to identify the parent cluster as follows: Columba-Horologium-Tucana: 42 ± 6 Myr, AB Doradus: 120 ± 10 Myr, Pleiades: 125 ± 8 Myr, Hercules-Lyra: 257 ± 46 Myr, Coma Berenices: 584 ± 10 Myr, Hyades: 625 ± 50 Myr.

Case	Type	Age (Myr)	M (M_{\odot})	R (R_{\odot})	P_{rot} (d)	B_r (G)	R_A (R_{\star})	\dot{M}_w (kg s^{-1})	$7 \times \dot{J}_w$ (Nm)	I (kg m^2)
1 CI Melotte 25 5	K0	625± 50	0.85	0.91	10.57	6.0	12.0	4.95×10^9	7.80×10^{24}	3.66×10^{46}
2 CI Melotte 25 21	G5	625± 50	0.90	0.91	9.73	10.0	14.4	7.54×10^9	1.68×10^{25}	4.27×10^{46}
3 CI Melotte 25 43	K0	625± 50	0.85	0.79	9.90	5.8	12.4	3.31×10^9	4.68×10^{24}	2.79×10^{46}
4 CI Melotte 25 151	K2	625± 50	0.85	0.82	10.41	10.9	13.8	6.61×10^9	9.92×10^{24}	2.97×10^{46}
5 CI Melotte 25 179	K0	625± 50	0.85	0.84	9.70	17.0	16.2	1.05×10^{10}	2.35×10^{25}	3.11×10^{46}
6 TYC 1987-509-1	K2	584± 10	0.80	0.72	11.10	10.1	12.9	4.10×10^9	3.47×10^{24}	1.94×10^{46}
7 CI* Melotte 111 AV 1693	G8	584± 10	0.90	0.83	9.05	20.3	14.8	1.15×10^{10}	2.25×10^{25}	3.62×10^{46}
8 CI* Melotte 111 AV 1826	G9	584± 10	0.85	0.80	9.34	12.6	12.7	7.33×10^9	8.50×10^{24}	2.84×10^{46}
9 CI* Melotte 111 AV 2177	G6	584± 10	0.90	0.78	8.98	5.5	11.7	2.76×10^9	3.86×10^{24}	3.13×10^{46}
10 CI* Melotte 111 AV 523	G7	584± 10	0.90	0.83	9.43	14.6	14.0	8.27×10^9	1.33×10^{25}	3.56×10^{46}
11 DX Leo	G9	257± 46	0.90	0.81	5.38	21.1	17.8	1.14×10^{10}	5.65×10^{25}	3.42×10^{46}
12 EP Eri	K1	257± 46	0.85	0.72	6.76	9.5	11.7	3.97×10^9	5.85×10^{24}	2.28×10^{46}
13 HH Leo	G8	257± 46	0.95	0.84	5.92	15.3	15.8	9.32×10^9	3.65×10^{25}	4.26×10^{46}
14 V439 And	K0	257± 46	0.95	0.92	6.23	8.7	13.4	6.85×10^9	1.87×10^{25}	5.05×10^{46}
15 V447 Lac	K1	257± 46	0.90	0.81	4.43	10.4	12.6	5.84×10^9	1.40×10^{25}	3.42×10^{46}
16 HII 296	G8	125± 8	0.90	0.94	2.61	51.4	22.5	3.14×10^{10}	3.42×10^{26}	4.50×10^{46}
17 HII 739	G0	125± 8	1.15	1.07	1.56	49.6	16.3	3.67×10^{10}	8.20×10^{26}	1.13×10^{47}
18 CI* Melotte 22 PELS 31	K2 [†]	125± 8	0.95	1.05	2.50	17.0	11.8	1.71×10^{10}	1.01×10^{26}	6.58×10^{46}
19 BD-07 2388	K0	120± 10	0.85	0.78	0.33	94.2	30.2	3.54×10^{10}	2.23×10^{27}	2.66×10^{46}
20 HD 6569	K1	120± 10	0.85	0.76	7.13	15.3	16.1	7.36×10^9	1.71×10^{25}	2.50×10^{46}
21 HIP 10272	K1	120± 10	0.90	0.80	6.13	10.1	14.5	5.11×10^9	1.44×10^{25}	3.29×10^{46}
22 HIP 76768	K5	120± 10	0.80	0.85	3.70	58.6	23.1	3.05×10^{10}	2.02×10^{26}	2.66×10^{46}
23 LO Peg (HIP 106231)	K3	120± 10	0.75	0.66	0.42	88.6	29.0	2.19×10^{10}	8.13×10^{26}	1.34×10^{46}
24 PW And	K2	120± 10	0.85	0.78	1.76	70.7	24.7	2.49×10^{10}	3.90×10^{26}	2.68×10^{46}
25 TYC 0486-4943-1	K4 [†]	120± 10	0.77	0.70	3.75	18.7	14.9	8.61×10^9	3.25×10^{25}	1.61×10^{46}
26 TYC 5164-567-1	K1 [†]	120± 10	0.90	0.90	4.68	48.5	21.6	2.96×10^{10}	1.68×10^{26}	4.13×10^{46}
27 BD-16 351	K1 [†]	42± 6	0.90	0.96	3.21	32.8	20.5	2.37×10^{10}	3.08×10^{26}	5.07×10^{46}
28 Sun CR2157 (solar maximum)	G2	4600	1.00	1.00	25.38	5.6	6.9	3.84×10^9	7.95×10^{23}	7.06×10^{46}
29 Sun CR2211 (solar minimum)	G2	4600	1.00	1.00	25.38	0.6	5.0	3.94×10^8	5.55×10^{22}	7.06×10^{46}

Table 2. Wind modelling parameters used for all the stellar and solar models used in this work. The parameters that vary between wind models are the surface magnetic map, stellar rotation rate, mass, and radius. All other modelling parameters are fixed. Note that the stellar age is not a wind model input.

Parameter	Value
Stellar surface magnetic map	See Folsom et al. (2016, 2018)
Stellar rotation rate	Table 1
Stellar mass	Table 1
Stellar radius	Table 1
Chromospheric base temperature	5.0×10^4 K
Chromospheric base density	$2.0 \times 10^{17} \text{ m}^{-3}$
Poynting flux-to-field ratio	$1.1 \times 10^6 \text{ W m}^{-2} \text{ T}^{-1}$
Turbulence correlation length	$1.5 \times 10^5 \text{ m T}^{1/2}$

3 DISCUSSION

Multiple, possibly interacting physical phenomena have been proposed as causes for the torque saturation in rapid rotators. These

Table 3. Fitted coefficients for the broken power law $y/y_{\text{sat}} = (\Omega/\Omega_{\text{sat}})^a$. The first two numerical columns give the exponent a values on either side of the saturation point $\Omega_{\text{sat}} = 8.9 \Omega_{\odot}$. The final column gives the value of $\log_{10} y_{\text{sat}}$ for $y_{\text{sat}} = y(\Omega_{\text{sat}})$. The first three of these relationships are plotted in Fig. 2. The average Alfvén radius R_A is plotted in Fig. A1. The coefficient of determination r^2 is given in the final column.

Quantity	a ($\Omega > \Omega_{\text{sat}}$)	a ($\Omega < \Omega_{\text{sat}}$)	$\log_{10} y_{\text{sat}}$	r^2
$\Omega/\dot{\Omega}_w$ (Myr)	-0.01 ± 0.30	-2.17 ± 0.17	2.01 ± 0.04	0.72
\dot{J}_w (Nm)	0.85 ± 0.27	3.02 ± 0.15	26.42 ± 0.04	0.87
\dot{M} (kg s^{-1})	0.09 ± 0.13	1.30 ± 0.07	10.39 ± 0.02	0.70
Φ (Wb)	0.29 ± 0.13	1.25 ± 0.07	16.25 ± 0.02	0.70
B_r (G)	0.39 ± 0.12	1.31 ± 0.07	1.62 ± 0.02	0.74
R_A (R)	0.14 ± 0.02	0.49 ± 0.01	1.33	0.75

include a decoupling mechanism where the stellar convective zone may rotate at a different rate than the radiative zone (Stauffer & Hartmann 1986; MacGregor & Brenner 1991) while exchanging angular momentum with the interior (Bouvier 2008; Gallet & Bouvier 2013,

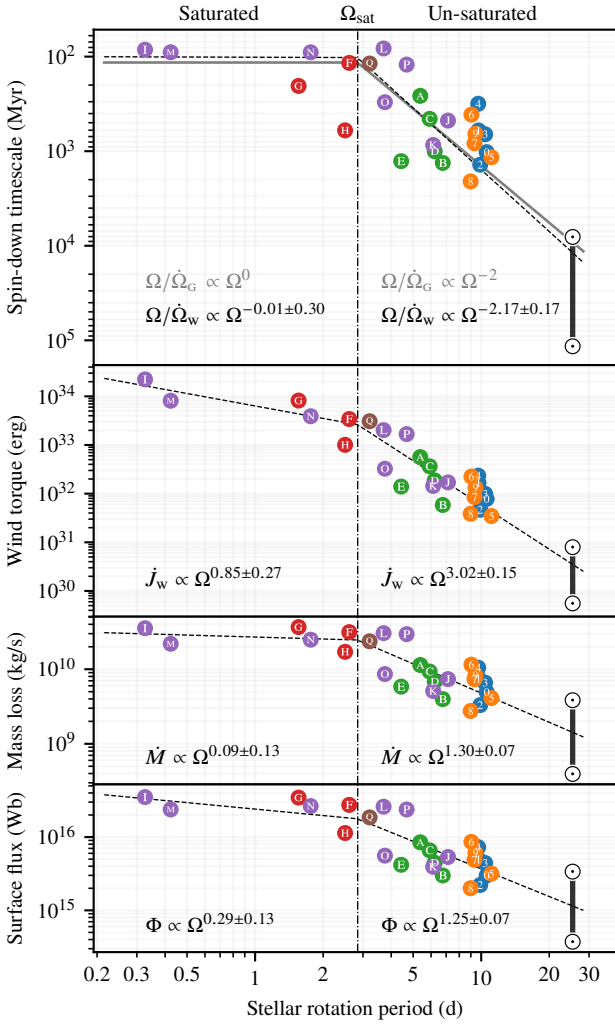


Figure 2. In the top panel we compare the spin-down timescale inferred from the wind models $\Omega/\dot{\Omega}_w$ (coloured symbols) and the spin-down timescale $\Omega/\dot{\Omega}_{\text{obs}}$ (grey curve) from equation (2). The two Sun symbols connected by a black bar represents the solar maximum and minimum. The second panel shows the wind torque \dot{J}_w (1 erg = 10^{-7} N m) and the third panel shows the wind mass loss rate \dot{M}_w values (the commonly used solar mass loss rate value is $2 \times 10^{-14} M_{\odot} \text{ yr}^{-1} = 1 \times 10^9 \text{ kg s}^{-1}$). The bottom panels show the surface unsigned magnetic flux Φ which is determined directly from the magnetic maps driving the numerical models. The dashed black lines show the broken power law fit of equation (3). The vertical dash-dotted line shows $\Omega_{\text{sat}} = 8.9 \Omega_{\odot}$ which separates the saturated ($\Omega > \Omega_{\text{sat}}$) and un-saturated ($\Omega < \Omega_{\text{sat}}$) spin-down regimes.

2015). Another cause could be a change in the nature of emerging photospheric magnetic field and/or the stellar corona (Vilhu 1984; Pizzolato et al. 2003; Wright et al. 2011; Reiners & Mohanty 2012; Marsden et al. 2014) around Ω_{sat} . MacGregor & Brenner (1991), for example, suggested that the surface magnetic field strength B may saturate in rapid rotators. Alternatively, the knee could be a consequence of a change in the magnetic field complexity (Garraffo et al. 2015, 2018; Finley & Matt 2018). See et al. (2019), however, found that that field complexity plays a modest role for reasonable mass-loss rates.

In Fig. 2 we see that the plotted quantities $\Omega/\dot{\Omega}_w$, \dot{J}_w , \dot{M}_w and Φ exhibit a similar structure, in which the quantity saturates for $\Omega \gtrsim \Omega_{\text{sat}}$. This suggests that the saturation of the wind torque and

wind mass loss rate is a consequence of the saturation of the surface unsigned magnetic flux Φ in our models. The result is consistent with the findings of Evensberger et al. (2023) where no break was found when considering \dot{J}_w and \dot{M} as a function of surface unsigned magnetic flux or field complexity, and the residual spread was attributed to stellar magnetic cycles. We thus attribute the saturation in Fig. 2 to a saturation in the surface unsigned magnetic flux (and surface magnetic field strength since $\Phi = 4\pi R^2 B_r$) for $\Omega \gtrsim \Omega_{\text{sat}}$. The mass loss rate \dot{M} saturation arises naturally in our models, while mass loss rate saturation at high rates of rotation is externally imposed in many models of spin-down (Gallet & Bouvier 2013, 2015; Johnstone et al. 2015; Sadeghi Ardestani et al. 2017; Ahuir et al. 2020). Such mass loss rate saturation may (or may not) have observational support (Vidotto 2021; Wood et al. 2021). In the Alfvén wave based model used in this work there is an approximate power-law relationship between \dot{M} and Φ (Evensberger et al. 2023) which means that the mass loss rate saturation is a consequence of magnetic saturation. Similar mass loss rate saturation may be seen also in the one-dimensional Alfvén wave based model of Cranmer & Saar (2011), and in the models of Suzuki (2011); Suzuki et al. (2013); Shoda et al. (2020).

Stellar magnetic activity is known to saturate with increasing rotation (Noyes et al. 1984; Pizzolato et al. 2003) and there are signs of saturation of the surface magnetic field strength (Reiners et al. 2009; Vidotto et al. 2014). This is supported by the saturation in spot filling factors found by Cao & Pinsonneault (2022). Early models (MacGregor & Brenner 1991) suggested that that $B \propto \Omega^a$ where $a \approx 1$ (linear dynamo) in the un-saturated regime and ≈ 0 (saturated dynamo) in the saturated regime. In our dataset we find that the surface unsigned magnetic flux in the un-saturated regime $\Phi \propto \Omega^{1.25 \pm 0.07}$ is matched by the $B_r \propto \Omega^{1.32 \pm 0.14}$ result of Vidotto et al. (2014). In comparison with the spin-down timescale and mass loss rate values, the surface unsigned magnetic flux appears to continue increasing past Ω_{sat} , albeit at a slower rate as in Reiners et al. (2014, 2022).

We have applied a scaling on the wind torque values \dot{J}_w in order to match the gyrotrack torque \dot{J}_{obs} at solar maximum. In our work the scaling factor has the same value of 7 for all the stars modelled (and the Sun), and is thus independent of Ω . Similar torque scalings have a long history in the literature (Krishnamurthi et al. 1997). Solar wind torque estimates based on the solar surface magnetic field strength can be ~ 20 times smaller than the torque required by the Skumanich relation and the $\Omega_{\text{obs}}(t)$ gyrotracks (Finley & Matt 2018; Finley et al. 2018). In See et al. (2019) the torque values of Finley & Matt (2018) were scaled by ~ 25 to match the gyrotracks of Matt et al. (2015). Similarly, the Matt et al. (2012) wind torque formula, which was used in the Gallet & Bouvier (2013) gyrotracks and by Johnstone et al. (2015) was scaled by a factor of ~ 2 and ~ 11 respectively to match cluster rotation rate observations. In this work, we find that a single, constant $7 \times$ torque scaling factor is sufficient for our Alfvén based wind model to agree with observations.

The need for the $7 \times$ torque scaling may be rooted in underestimates of the stellar magnetic field strengths (Morin et al. 2010; Yadav et al. 2015; Lehmann et al. 2019) and solar magnetic field strengths, the latter in which a scaling of 2–4 is often applied to match the measured magnetic field at 1 au (Cohen et al. 2006; Oran et al. 2013; Linker et al. 2017; Pognan et al. 2018; Finley et al. 2018; Sachdeva et al. 2019; Riley et al. 2021). Zeeman-Doppler imaging reconstructs large-scale magnetic features on the stellar surface in an Ω -dependent way (Hussain et al. 2000; Morin et al. 2010), but only a fraction of the field strength is recovered (e.g. Lehmann et al. 2019). These two biases may be used to justify a scaling of \dot{J}_w including the $7 \times$ scaling applied in this work. On a similar note we find that scaling the surface magnetic field by a factor of ~ 5 as in Evensberger et al.

(2021, 2022, 2023) we also obtain gyrotracks with both exponential and Skumanich-type spin-down. We do not pursue this alternative approach here as the resulting wind mass loss rate values differ for the solar case (see Evensberget et al. 2023). We do however emphasise that the qualitative indications of a saturated and an un-saturated magnetic regime also appear in this model series.

Alternatively, the need for the $7\times$ torque scaling may be attributed to core-envelope decoupling (Stauffer & Hartmann 1986; Denisov et al. 2010; Gallet & Bouvier 2013, 2015), where the stellar convective envelope may spin at a different rate than the core while exchanging rotational momentum with it at a (configurable) coupling timescale τ . Core-envelope decoupling would change the direction of the coloured arrows in Fig. 1 and, depending on the length of τ , it could have the same effect as changing the torque scaling factor or scaling the ZDI magnetic field strength. A variable τ was invoked by Gallet & Bouvier (2013, 2015) to create their observed-based gyrotracks extending from the stellar contraction era to the Sun's age. In the Baraffe et al. (2015) models $\sim 20\%$ of our stars' rotational inertia is in the envelope. This could produce an effect similar to required torque scaling for long τ , in that the envelope spins down with little angular momentum exchange with the core in parts of the stars' life. Core-envelope decoupling has theoretical support from hydrodynamic modelling (Endal & Sofia 1981; Rucinski 1988; Pisonneault et al. 1989; Zahn 1992; Amard et al. 2016, 2019) but it has been suggested that the inclusion of magnetohydrodynamic instabilities such as the Tayler (1973) instability may effectively flatten the internal rotation curve (Fuller et al. 2019; Eggenberger et al. 2022). Some models of stellar spin-down (Collier Cameron & Li 1994; Matt et al. 2015; Johnstone et al. 2015) have applied a model of solid body rotation. The recently discovered 'stalled spin-down' (Agüeros et al. 2018; Curtis et al. 2019; Douglas et al. 2019; David et al. 2022) of K dwarfs is however attributed to core-envelope decoupling (e.g. Spada & Lanzafame 2020; Cao et al. 2022, 2023), although a magnetic wind effect may also play a role (Curtis et al. 2020).

4 CONCLUSIONS

We have modelled the stellar spin-down rates of 27 young, solar-type stars based on wind models published in Evensberget et al. (2021, 2022, 2023) and whose surface magnetic fields were reconstructed by Folsom et al. (2016, 2018) using Zeeman-Doppler imaging. We have compared our resulting wind torques and spin-down rates with the observation-based $\Omega(t)$ gyrotracks of Gallet & Bouvier (2013).

Unlike many previous works, our wind torques are derived from fully three-dimensional wind models where the corona is heated by Alfvén waves. As our wind model (Sokolov et al. 2013; van der Holst et al. 2014) extends into the chromosphere, the coronal density and temperature emerge naturally as a consequence of the coronal heating by Alfvén wave turbulence. This means that we do not need to impose a desired mass loss rate by adjusting the coronal density, as is required in polytropic wind models (Vidotto et al. 2009; Matt et al. 2012; Réville et al. 2015; Finley & Matt 2017; Finley et al. 2018). Instead, the mass loss rate emerges naturally as a consequence of the coronal heating, and ultimately the surface magnetic field strength.

We find that the torque and the mass loss rate produced by our wind model (using the same solar configuration parameters across the entire age and rotation rate range) are compatible with features of the observationally derived gyrotracks $\Omega_{\text{obs}}(t)$ for both fast and slow rotators from the onset of the spin-down era until the Sun's age. We find signs of both the exponential ($\dot{\Omega} \propto \Omega$) spin-down rate for rapid rotators and the Skumanich-type ($\dot{\Omega} \propto \Omega^3$) spin-down rate for

slow rotators. In our models the two regimes arise as a consequence of the ZDI observed magnetic field strength saturation at rapid rates of rotation.

Our model is novel as it uses only a single free scaling parameter in order to agree with observations. By scaling all the wind torque based spin-down rates $\dot{\Omega}_w$ by a factor of 7, so that the solar maximum value matches the $\dot{\Omega}_\odot$ value predicted from the Skumanich (1972) relation $\Omega \propto t^{-1/2}$, we find good agreement between the gyrotrack-derived spin-down time-scales $\Omega/\dot{\Omega}_{\text{obs}}$ and the wind torque-derived spin-down time-scales $\Omega/\dot{\Omega}_w$. Such scalings have long been used in evolutionary models (e.g. Krishnamurthi et al. 1997). The scaling may be needed because of changes in the effective rotational inertia due to core-envelope decoupling, or due to ZDI underestimates of the unsigned magnetic flux; both effects would lead to an increase in $\dot{\Omega}_w$.

Our work suggests that the wind torque saturation is caused by a saturation of the surface magnetic field *strength*, rather than a qualitative change in the magnetic field complexity for rapidly rotating stars. To further confirm or refute our findings it would be necessary to have more ZDI data of stars with very well constrained ages. ZDI data of stars with rotation periods in the range 0.2 d to 1 d and > 10 d would be of particular interest.

ACKNOWLEDGEMENTS

This project has received funding from the European Research Council (ERC) under the European Union's Horizon 2020 research and innovation programme (grant agreement No 817540, ASTROFLOW). This work used the Dutch national e-infrastructure with the support of the SURF Cooperative using grant nos. EINF-2218 and EINF-5173. This research has made use of NASA's *Astrophysics Data System*. This work was carried out using the *swmf* tools developed at The University of Michigan *Center for Space Environment Modelling (CSEM)* and made available through the NASA *Community Coordinated Modelling Center (CCMC)*. This work has made use of the following additional numerical software, statistics software and visualisation software: NumPy (van der Walt et al. 2011), SciPy (Virtanen et al. 2020), Matplotlib (Hunter 2007), and statsmodels (Seabold & Perktold 2010). We would like to express our gratitude to the anonymous reviewers for their valuable contributions, which have enhanced the quality and rigour of our article.

DATA AVAILABILITY

The data underlying this article will be shared on reasonable request to the corresponding author.

REFERENCES

- Agüeros M. A., et al., 2018, *ApJ*, **862**, 33
 Ahuir J., Brun A. S., Strugarek A., 2020, *A&A*, **635**, A170
 Airapetian V. S., Jin M., Lüftinger T., Boro Saikia S., Kochukhov O., Güdel M., Van Der Holst B., Manchester W. I., 2021, *ApJ*, **916**, 96
 Alvarado-Gómez J. D., Hussain G. A. J., Cohen O., Drake J. J., Garraffo C., Grunhut J., Gombosi T. I., 2016, *A&A*, **588**, A28
 Amard L., Palacios A., Charbonnel C., Gallet F., Bouvier J., 2016, *A&A*, **587**, A105
 Amard L., Palacios A., Charbonnel C., Gallet F., Georgy C., Lagarde N., Siess L., 2019, *A&A*, **631**, A77
 Baraffe I., Homeier D., Allard F., Chabrier G., 2015, *A&A*, **577**, A42

- Boro Saikia S., Jin M., Johnstone C. P., Lüftinger T., Güdel M., Airapetian V. S., Kislyakova K. G., Folsom C. P., 2020, *A&A*, **635**, A178
- Bouvier J., 1991, in Catalano S., Stauffer J. R., eds, NATO Advanced Study Institute (ASI) Series C Vol. 340, Angular Momentum Evolution of Young Stars. Springer, Dordrecht, p. 41
- Bouvier J., 2008, *A&A*, **489**, L53
- Cao L., Pinsonneault M. H., 2022, *MNRAS*, **517**, 2165
- Cao L., Pinsonneault M. H., Hillenbrand L. A., Kuhn M. A., 2022, *ApJ*, **924**, 84
- Cao L., Pinsonneault M. H., van Saders J. L., 2023, *ApJ*, **951**, L49
- Chaboyer B., Demarque P., Pinsonneault M. H., 1995, *ApJ*, **441**, 865
- Cohen O., 2017, *ApJ*, **835**, 220
- Cohen O., Fisk L. A., Roussev I. I., Toth G., Gombosi T. I., 2006, *ApJ*, **645**, 1537
- Collier Cameron A., Li J., 1994, *MNRAS*, **269**, 1099
- Cox A. N., 2000, Allen's astrophysical quantities. Springer Science & Business Media
- Cranmer S. R., Saar S. H., 2011, *ApJ*, **741**, 54
- Curtis J. L., Agüeros M. A., Douglas S. T., Meibom S., 2019, *ApJ*, **879**, 49
- Curtis J. L., et al., 2020, *ApJ*, **904**, 140
- David T. J., Angus R., Curtis J. L., van Saders J. L., Colman I. L., Contardo G., Lu Y., Zinn J. C., 2022, *ApJ*, **933**, 114
- Denissenkov P. A., Pinsonneault M., Terndrup D. M., Newsham G., 2010, *ApJ*, **716**, 1269
- Douglas S. T., Curtis J. L., Agüeros M. A., Cargile P. A., Brewer J. M., Meibom S., Jansen T., 2019, *ApJ*, **879**, 100
- Drajer N. R., 1998, Applied regression analysis. Wiley Series in Probability, Wiley
- Durney B. R., Latour J., 1978, Geophysical and Astrophysical Fluid Dynamics, **9**, 241
- Edwards S., et al., 1993, *AJ*, **106**, 372
- Eggenberger P., Buldgen G., Salmon S. J. A. J., Noels A., Grevesse N., Asplund M., 2022, *Nature Astronomy*, **6**, 788
- Endal A. S., Sofia S., 1981, *ApJ*, **243**, 625
- Evensberget D., Carter B. D., Marsden S. C., Brookshaw L., Folsom C. P., 2021, *MNRAS*, **506**, 2309
- Evensberget D., Carter B. D., Marsden S. C., Brookshaw L., Folsom C. P., Salmeron R., 2022, *MNRAS*, **510**, 5226
- Evensberget D., Carter B. D., Marsden S. C., Brookshaw L., Folsom C. P., Salmeron R., 2023, *MNRAS*
- Finley A. J., Matt S. P., 2017, *ApJ*, **845**, 46
- Finley A. J., Matt S. P., 2018, *ApJ*, **854**, 78
- Finley A. J., Matt S. P., See V., 2018, *ApJ*, **864**, 125
- Folsom C. P., et al., 2016, *MNRAS*, **457**, 580
- Folsom C. P., et al., 2018, *MNRAS*, **474**, 4956
- Fuller J., Piro A. L., Jermyn A. S., 2019, *MNRAS*, **485**, 3661
- Gallet F., Bouvier J., 2013, *A&A*, **556**, A36
- Gallet F., Bouvier J., 2015, *A&A*, **577**, A98
- Garraffo C., Drake J. J., Cohen O., 2015, *ApJ*, **807**, L6
- Garraffo C., et al., 2018, *ApJ*, **862**, 90
- Godoy-Rivera D., Pinsonneault M. H., Rebull L. M., 2021, *ApJS*, **257**, 46
- Gombosi T. I., van der Holst B., Manchester W. B., Sokolov I. V., 2018, *Living Reviews in Solar Physics*, **15**, 4
- Gombosi T. I., et al., 2021, *Journal of Space Weather and Space Climate*, **11**, 42
- Huang Z., Tóth G., Sachdeva N., Zhao L., van der Holst B., Sokolov I., Manchester W. B., Gombosi T. I., 2023, *ApJ*, **946**, L47
- Hunter J. D., 2007, *Computing in Science and Engineering*, **9**, 90
- Hussain G. A. J., Donati J. F., Collier Cameron A., Barnes J. R., 2000, *MNRAS*, **318**, 961
- Johnstone C. P., Güdel M., Brott I., Lüftinger T., 2015, *A&A*, **577**, A28
- Kawaler S. D., 1988, *ApJ*, **333**, 236
- Krishnamurthi A., Pinsonneault M. H., Barnes S., Sofia S., 1997, *ApJ*, **480**, 303
- Lehmann L. T., Hussain G. A. J., Jardine M. M., Mackay D. H., Vidotto A. A., 2019, *MNRAS*, **483**, 5246
- Linker J. A., et al., 2017, *ApJ*, **848**, 70
- MacGregor K. B., Brenner M., 1991, *ApJ*, **376**, 204
- Marsden S. C., et al., 2014, *MNRAS*, **444**, 3517
- Matt S. P., MacGregor K. B., Pinsonneault M. H., Greene T. P., 2012, *ApJ*, **754**, L26
- Matt S. P., Brun A. S., Baraffe I., Bouvier J., Chabrier G., 2015, *ApJ*, **799**, L23
- Mestel L., 1968, *MNRAS*, **140**, 177
- Mestel L., 1984, Angular Momentum Loss During Pre-Main Sequence Contraction. Springer, Berlin, Heidelberg, p. 49, doi:10.1007/3-540-12907-3_179
- Morin J., Donati J.-F., Petit P., Delfosse X., Forveille T., Jardine M. M., 2010, *MNRAS*, **407**, 2269
- Noyes R. W., Hartmann L. W., Baliunas S. L., Duncan D. K., Vaughan A. H., 1984, *ApJ*, **279**, 763
- Oran R., van der Holst B., Landi E., Jin M., Sokolov I. V., Gombosi T. I., 2013, *The Astrophysical Journal*, **778**, 176
- Parker E. N., 1958, *ApJ*, **128**, 664
- Pecaut M. J., Mamajek E. E., 2013, *ApJS*, **208**, 9
- Pinsonneault M. H., Kawaler S. D., Sofia S., Demarque P., 1989, *ApJ*, **338**, 424
- Pizzoloto N., Maggio A., Micela G., Sciortino S., Ventura P., 2003, *A&A*, **397**, 147
- Pognan Q., Garraffo C., Cohen O., Drake J. J., 2018, *ApJ*, **856**, 53
- Powell K. G., Roe P. L., Linde T. J., Gombosi T. I., De Zeeuw D. L., 1999, *Journal of Computational Physics*, **154**, 284
- Reiners A., Mohanty S., 2012, *ApJ*, **746**, 43
- Reiners A., Basri G., Browning M., 2009, *ApJ*, **692**, 538
- Reiners A., Schüssler M., Passegger V. M., 2014, *ApJ*, **794**, 144
- Reiners A., et al., 2022, *A&A*, **662**, A41
- Réville V., Brun A. S., Matt S. P., Strugarek A., Pinto R. F., 2015, *ApJ*, **798**, 116
- Riley P., Lionello R., Caplan R. M., Downs C., Linker J. A., Badman S. T., Stevens M. L., 2021, *A&A*, **650**, A19
- Rucinski S. M., 1988, *AJ*, **95**, 1895
- Sachdeva N., et al., 2019, *ApJ*, **887**, 83
- Sadeghi Ardestani L., Guillot T., Morel P., 2017, *MNRAS*, **472**, 2590
- Schatzman E., 1962, *Annales d'Astrophysique*, **25**, 18
- Seabold S., Perktold J., 2010, in 9th Python in Science Conference. SciPy proceedings, Austin Texas
- See V., et al., 2019, *ApJ*, **886**, 120
- Shoda M., et al., 2020, *ApJ*, **896**, 123
- Skumanich A., 1972, *ApJ*, **171**, 565
- Sokolov I. V., et al., 2013, *ApJ*, **764**, 23
- Spada F., Lanzafame A. C., 2020, *A&A*, **636**, A76
- Stauffer J. B., Hartmann L. W., 1986, *PASP*, **98**, 1233
- Stauffer J. R., Hartmann L. W., 1987, *ApJ*, **318**, 337
- Stauffer J. R., Hartmann L. W., Burnham J. N., Jones B. F., 1985, *ApJ*, **289**, 247
- Suzuki T. K., 2011, *Space Sci. Rev.*, **158**, 339
- Suzuki T. K., Imada S., Kataoka R., Kato Y., Matsumoto T., Miyahara H., Tsuneta S., 2013, *PASJ*, **65**, 98
- Taylor R. J., 1973, *MNRAS*, **161**, 365
- Tóth G., et al., 2005, *Journal of Geophysical Research (Space Physics)*, **110**, A12226
- Tóth G., et al., 2012, *Journal of Computational Physics*, **231**, 870
- Vidotto A. A., 2021, *Living Reviews in Solar Physics*, **18**, 3
- Vidotto A. A., Opher M., Jatenco-Pereira V., Gombosi T. I., 2009, *ApJ*, **699**, 441
- Vidotto A. A., et al., 2014, *MNRAS*, **441**, 2361
- Vidotto A. A., Bourrier V., Fares R., Bellotti S., Donati J. F., Petit P., Hussain G. A. J., Morin J., 2023, *A&A*, **678**, A152
- Vilhu O., 1984, *A&A*, **133**, 117
- Virtanen P., et al., 2020, *Nature Methods*, **17**, 261
- Weber E. J., Davis Jr. L., 1967, *ApJ*, **148**, 217
- Wood B. E., et al., 2021, *ApJ*, **915**, 37
- Wright N. J., Drake J. J., Mamajek E. E., Henry G. W., 2011, *ApJ*, **743**, 48
- Yadav R. K., Christensen U. R., Morin J., Gastine T., Reiners A., Poppenthaler K., Wolk S. J., 2015, *ApJ*, **813**, L31
- Zahn J. P., 1992, *A&A*, **265**, 115

van der Holst B., Sokolov I. V., Meng X., Jin M., Manchester W. B. I., Tóth G., Gombosi T. I., 2014, *The Astrophysical Journal*, 782, 81
 van der Walt S., Colbert S. C., Varoquaux G., 2011, *Computing in Science and Engineering*, 13, 22

APPENDIX A: WIND MODELS

This work is based upon numerical modelling carried out in Evensberget et al. (2021, 2022, 2023) where we used the Zeeman-Doppler imaging observations and surface magnetic maps of Folsom et al. (2016, 2018) to drive a three-dimensional numerical wind model incorporating Alfvén wave heating of the corona (the Alfvén wave solar model AWSOM, Sokolov et al. 2013; van der Holst et al. 2014). Table 1 gives the relevant stellar parameters used in our modelling, as well as key results from the wind modelling.

The AWSOM model is part of the block-adaptive tree solarwind Roe upwind scheme BATS-R-US (Powell et al. 1999; Tóth et al. 2005) and the space weather modelling framework SWMF (Tóth et al. 2012; Gombosi et al. 2021)⁴. In the AWSOM model the corona is heated by the dissipation of Alfvén wave energy in the form of an Alfvén wave energy flux emanating from the chromospheric base. The numerical wind models extend from the chromosphere to about 1 au.

At the inner boundary the chromospheric temperature is set to $T = 5 \times 10^4$ K and the number density is set to $n = 2 \times 10^{17} \text{ m}^{-3}$ (following e.g. Gombosi et al. 2018). These values are used for all our model runs (as described in Table 2).

The parameters given here are tuned to reproduce solar wind conditions. In contrast to polytropic wind models, the Alfvén wave based wind model (Sokolov et al. 2013; van der Holst et al. 2014) effectively shifts the model boundary downwards into the much colder and denser stellar chromosphere, making the coronal density and temperature more dependent on the Alfvén wave based heating model than on the chromospheric boundary conditions. This also permits the consistent computation of the coronal wind density and \dot{M} consistently with \dot{J} and R_A (e.g. Garraffo et al. 2015; Alvarado-Gómez et al. 2016; Cohen 2017).

The Alfvén wave energy flux across the stellar surface is proportional to the local magnetic field value (van der Holst et al. 2014). The proportionality constant Π_A/B is set to $1.1 \times 10^6 \text{ W m}^{-2} \text{ T}^{-1}$ which is the standard value used for the Sun and solar-type stars (Gombosi et al. 2018). We note that the Alfvén wave flux applied at the model boundary affects \dot{M} and \dot{J} differently (Boro Saikia et al. 2020; Airapetian et al. 2021; Huang et al. 2023; Vidotto et al. 2023). By scaling the Alfvén wave flux and the magnetic field strength \dot{M} can be varied while \dot{J} remains constant. Recently, the solar Alfvén flux-to-field ratio has been found to be correlated with the area of open field regions (Huang et al. 2023). The study also finds the parameter is anti-correlated with the average unsigned radial field in the open regions. Given the relation between \dot{M} and Π_A/B of Boro Saikia et al. (2020) this would reduce the span of \dot{M} by a factor of ~ 4 for the solar mass loss shown in Fig. 2. Future observations of chromospheric turbulence and solar modelling may justify such a similar scaling approach for stellar winds.

⁴ The open source version of the space weather modelling framework can be found on-line at <https://github.com/MSTEM-QUDA/SWMF.git>. In this work version 2.40.a5beb110f (2022-10-08) has been used for all processing.

A1 Stellar wind model input data

The following fundamental stellar parameters are varied between models: the stellar mass M , radius R , and rotation period $P_{\text{rot}} = 2\pi/\Omega$. In our work these values are taken from Folsom et al. (2016, 2018) and provided for convenience in Table 1. The stellar type and age in Table 1 are also from Folsom et al. (2016, 2018) but are not in any way part of the wind model input. The solar minimum and solar maximum models use processed GONG magnetograms of Carrington rotation 2211 and 2157 respectively (see Evensberget et al. 2021). The stellar mass, radius, and period of rotation values have uncertainties of $\lesssim 10\%$, $\lesssim 20\%$, and $\lesssim 10\%$. The period error is approximately equal to the width of the round symbols used to denote each star in Fig. 1, Fig. 2 and Fig. A1.

The surface magnetic maps, in the form of spherical harmonics coefficients of the radial magnetic field, are ingested into the model at the inner boundary. The maps of the radial magnetic components can be seen in Folsom et al. (2016, 2018), in which they were derived, and are also reproduced in Evensberget et al. (2021, 2022, 2023).

A2 Stellar wind model output data

As the AWSOM numerical model is relaxed towards a steady state, the non-radial magnetic field components are permitted to vary, while the radial magnetic field component stays fixed. Thus the average unsigned surface radial magnetic field B_r in Table 1 and the unsigned surface magnetic flux $\Phi = 4\pi R^2 B_r$ of Fig. 2 (bottom panel) stay fixed for each wind model.

The wind mass loss rate \dot{M} , wind angular momentum loss rate \dot{J}_w and average Alfvén radius R_A in Table 1 are computed from the wind model output in Evensberget et al. (2023) and briefly described here for convenience.

We find the wind mass loss rate \dot{M} by integrating over a sphere S centred on the star:

$$\dot{M} = \oint_S \rho \mathbf{u} \cdot \hat{\mathbf{n}} \, dS. \quad (\text{A1})$$

where ρ and \mathbf{u} are the local wind density and velocity values and $\hat{\mathbf{n}}$ is the normal of the surface S .

We compute the angular momentum loss rate \dot{J}_w from

$$\dot{J} = \oint_S (\mathbf{B} \times \mathbf{r})_3 \left(\frac{\mathbf{B} \cdot \hat{\mathbf{r}}}{\mu_0} \right) + (\Omega \varpi^2 + (\mathbf{r} \times \mathbf{v})_3) (\mathbf{v} \cdot \hat{\mathbf{r}}) \rho \, dS. \quad (\text{A2})$$

Here \mathbf{B} is the local vector magnetic field, μ_0 is the magnetic constant, $\varpi = \mathbf{r} - (\mathbf{r} \cdot \hat{\mathbf{z}})\hat{\mathbf{z}}$ denotes the cylindrical distance from the origin, and $\mathbf{v} = \mathbf{u} - \Omega \hat{\mathbf{z}} \times \mathbf{r}$ denotes the wind velocity in a co-rotating frame. $(\cdot)_3$ refers to the z component vector enclosed. The scalar angular velocity Ω is taken from Table 1.

We calculate the average Alfvén radius R_A by defining the radial distance to the Alfvén surface $r_A(\theta, \varphi)$ over each point θ, φ on the stellar surface. The average Alfvén radius (in stellar radii) is then given by

$$R_A = \frac{1}{4\pi R^2} \oint_S |r_A(\theta, \varphi)| \, dS. \quad (\text{A3})$$

where S is the stellar surface and R is the stellar radius from Table 1. R_A is thus the spherically averaged value of the distance to the Alfvén surface over the spherical surface parametrised by the polar and azimuthal coordinates (θ, φ) . Fig. A1 shows the average Alfvén radius R_A plotted against the stellar rotation period as in Fig. 2.

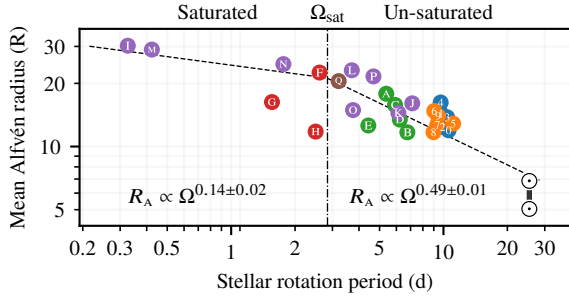


Figure A1. Mean Alfvén radius R_A plotted against the stellar rotation period as in Fig. 2. The fit parameters for R_A are given in Table 3.

APPENDIX B: SPIN-DOWN TIMESCALES

To compute the spin-down timescales $\Omega/\dot{\Omega}_w$ we use the scaled wind torque \dot{J}_w values from Evensberget et al. (2023) and the rotational inertia I from Baraffe et al. (2015). In this model the solar rotational inertia $I_\odot = 7.1 \times 10^{46} \text{ kg m}^2$. The exact values used for each star is given in Table 1. We note that there is some spread in reported solar rotational inertia values, as $I_\odot = 5.8 \times 10^{46} \text{ kg m}^2$ in e.g. Cox (2000).

The rotational inertia I values are not part of the wind model input, but are used to compute the spin-down timescales $\Omega/\dot{\Omega}_w$ as described in Section 2.1 with equation (1). Note that we do not consider the contraction torque term $\Omega\dot{I}$ in this work so that in effect $\dot{J}_w = \dot{\Omega}I$ in equation (1). In this work we also do not consider core-envelope decoupling (e.g. Stauffer & Hartmann 1986). The spin-down timescales $\Omega/\dot{\Omega}_w$ for each star are computed from the values given in Table 1. These values are also plotted in Fig. 1 and the top panel of Fig. 2.

Fig. B1 shows the residual ratio $\dot{\Omega}_w/\dot{\Omega}_{\text{obs}}$ for each star. The residual ratio is computed from the gyrotrack spin-down timescale $\Omega/\dot{\Omega}_{\text{obs}}$ and the wind spin-down timescale $\Omega/\dot{\Omega}_w$. The numerical values of $\Omega/\dot{\Omega}_{\text{obs}}$, $\Omega/\dot{\Omega}_w$, and $\dot{\Omega}_w/\dot{\Omega}_{\text{obs}}$ are given in Table B1. The dark, coloured bars in Figure B1 are 95 % confidence intervals of the mean $\dot{\Omega}_w/\dot{\Omega}_{\text{obs}}$ in each cluster. The confidence intervals are computed in the standard way (e.g. Draper 1998) using the Student's t distribution with $n - 1$ degrees of freedom, where n is the number of stars in each cluster. For the solar minimum and maximum models we do not compute or show a confidence interval as there is only one model for each of these cases. Similarly for \odot BD-16 351 no confidence interval can be computed as we only have one model aged 42 ± 6 Myr. The confidence interval parameters are given in Table B2.

The confidence intervals can be seen to cover the $\dot{\Omega}_w/\dot{\Omega}_{\text{obs}} = 1$ line in Fig. B1 for each of the clusters except the Hyades where the confidence interval ends just above the line. Tentatively, it appears that the Hercules-Lyra cluster (green symbols) has a lower $\dot{\Omega}_w/\dot{\Omega}_{\text{obs}}$ ratio than the other clusters. However, the confidence intervals are wide and the difference is not statistically significant. Similarly a trend of increasing $\dot{\Omega}_w/\dot{\Omega}_{\text{obs}}$ with age is not statistically significant. We attribute the residual spread in $\dot{\Omega}_w/\dot{\Omega}_{\text{obs}}$ to stellar magnetic cycles (see Evensberget et al. 2021) affecting the surface magnetic flux Φ (a source of scatter in the bottom panel of Fig. 2), but systematic errors in magnetogram detail with increasing Ω (Morin et al. 2010) may also play a role, as may stellar mass differences (see Table 1).

This paper has been typeset from a $\text{\TeX}/\text{\LaTeX}$ file prepared by the author.

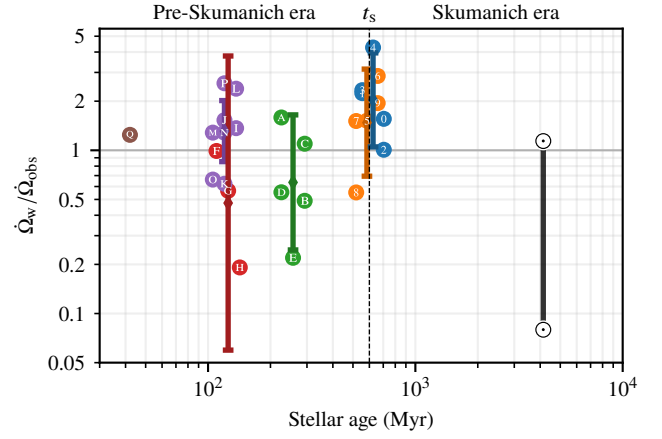


Figure B1. Residual ratio $\dot{\Omega}_w/\dot{\Omega}_{\text{obs}}$. The stellar symbol represent solar maximum and minimum. Values smaller than unity are associated with reduced rotational braking in Fig. 1. The dark vertical lines show 95 % confidence intervals for the average $\dot{\Omega}_w/\dot{\Omega}_{\text{obs}}$ in each cluster. Numerical values pertaining to this plot is given in Table B2.

Table B1. Spin-down timescales computed in this work, and the residual ratio between the gyro-track spin-down timescale and the wind spin-down timescale. The residual ratios are plotted against stellar age in in Fig. B1.

Case	$\Omega/\dot{\Omega}_{\text{obs}}$ (yr)	$\Omega/\dot{\Omega}_w$ (yr)	$\dot{\Omega}_w/\dot{\Omega}_{\text{obs}}$
① Mel25-5	1.60×10^9	1.02×10^9	1.56
② Mel25-21	1.35×10^9	6.04×10^8	2.24
③ Mel25-43	1.40×10^9	1.39×10^9	1.01
④ Mel25-151	1.55×10^9	6.63×10^8	2.34
⑤ Mel25-179	1.34×10^9	3.15×10^8	4.26
⑥ AV 523	1.76×10^9	1.16×10^9	1.52
⑦ AV 1693	1.17×10^9	4.10×10^8	2.85
⑧ AV 1826	1.25×10^9	8.24×10^8	1.51
⑨ AV 2177	1.15×10^9	2.09×10^9	0.55
⑩ TYC 1987	1.27×10^9	6.53×10^8	1.95
Ⓐ DX Leo	4.13×10^8	2.60×10^8	1.59
Ⓑ EP Eri	6.53×10^8	1.33×10^9	0.49
Ⓒ HH Leo	5.00×10^8	4.55×10^8	1.10
Ⓓ V439 And	5.54×10^8	1.00×10^9	0.55
Ⓔ V447 Lac	2.80×10^8	1.27×10^9	0.22
Ⓕ HII 296	1.15×10^8	1.17×10^8	0.99
Ⓖ HII 739	1.15×10^8	2.04×10^8	0.57
Ⓗ PELS 031	1.15×10^8	6.02×10^8	0.19
Ⓘ BD-072388	1.15×10^8	8.45×10^7	1.37
Ⓛ HD 6569	7.26×10^8	4.75×10^8	1.53
Ⓚ HIP 10272	5.37×10^8	8.60×10^8	0.62
Ⓛ HIP 76768	1.96×10^8	8.20×10^7	2.39
Ⓜ LO Peg	1.15×10^8	8.99×10^7	1.28
Ⓝ PW And	1.15×10^8	9.00×10^7	1.28
Ⓞ TYC 0486	2.01×10^8	3.03×10^8	0.66
Ⓟ TYC 5164	3.13×10^8	1.21×10^8	2.58
Ⓞ BD-16351	1.47×10^8	1.18×10^8	1.24
Ⓞ Sun CR2157	9.20×10^9	8.08×10^9	1.14
Ⓞ Sun CR2211	9.20×10^9	1.16×10^{11}	0.08

Table B2. Residual ratio statistics for each cluster. For each cluster of this study we give the age, followed by the (dimensionless) mean residual ratio $\dot{\Omega}_w/\dot{\Omega}_{\text{obs}}$ and the 95% confidence interval of the mean. These parameters can also be seen visualised in Fig. B1. In the solar case the range between our minimum and maximum models is $0.080 < \dot{\Omega}_w/\dot{\Omega}_{\text{obs}} < 1.14$.

Cluster	Age (Myr)	Residual ratio $\dot{\Omega}_w/\dot{\Omega}_{\text{obs}}$		
		2.5%	Mean	97.5%
● Col-Hor-Tuc	42 ± 6	—	1.24	—
● AB Doradus	120 ± 10	0.85	1.31	2.02
● Pleiades	125 ± 8	0.06	0.48	3.78
● Hercules-Lyra	257 ± 46	0.25	0.64	1.65
● Coma Berenices	584 ± 10	0.69	1.48	3.14
● Hyades	625 ± 50	1.05	2.04	3.95